

CH₃I low-*n* Rydberg states in supercritical atomic fluids near the critical point

Luxi Li ^{a,b}, Xianbo Shi ^{a,b}, C.M. Evans ^{a,b,*}, G.L. Findley ^c

^a*Department of Chemistry and Biochemistry, Queens College – CUNY, Flushing, NY 11367, United States*

^b*Department of Chemistry, Graduate Center – CUNY, New York, NY 10016, United States*

^c*Department of Chemistry, University of Louisiana at Monroe, Monroe, LA 71209, United States*

Abstract

Vacuum ultraviolet photoabsorption spectra of CH₃I 6*s* and 6*s*' Rydberg states doped into supercritical argon, krypton, and xenon perturbers were measured from low density to the density of the triple point liquid at noncritical temperatures and on an isotherm near the perturber critical temperature. A full line shape analysis of these spectra was performed using a single set of intermolecular potential parameters for each dopant/perturber system. The resulting perturber induced shift of the simulated adiabatic transition of the 6*s* and 6*s*' Rydberg states is presented as a function of perturber number density, and this shift illustrates a perturber critical point effect on the excitation energies of the molecular low-*n* Rydberg states.

Key words: VUV absorption, methyl iodide, critical point effect, low-*n* Rydberg states

1 Introduction

Low- n Rydberg states doped into dense fluids [1] represent an important probe for the investigation of solvation effects, especially in supercritical fluids [2]. Both atomic [3–5] and molecular [6–11] dopant low- n Rydberg states perturbed by dense gases have been studied previously. Recently, we have measured photoabsorption spectra of the xenon $6s$ and $6s'$ Rydberg states as a function of argon number density, and have shown that these states shift and broaden significantly from low perturber number density to the density of the triple point liquid [5]. We also provided a semi-classical statistical line shape analysis to simulate the experimental absorption spectra with a single set of intermolecular potential parameters, both at noncritical temperatures and on an isotherm near the critical isotherm of argon [5]. A standard moment analysis of the simulated primary Xe $6s$ and $6s'$ Rydberg transitions then yielded the perturber induced shift of the first moment for both of these transitions and showed a striking critical point effect near the critical temperature and density of argon [5].

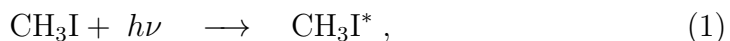
The molecular dopant CH_3I [6–8] has also been investigated extensively because of the “atomic” like nature of its $6s$ and $6s'$ Rydberg states. Messing *et al.* [6,7] extracted the perturber dependent shift $\Delta(\rho_P)$ [where ρ_P is the perturber number density] of the CH_3I $6s$ and $6s'$ Rydberg states by performing a moment analysis on the photoabsorption bands. This analysis indicated that $\Delta(\rho_P)$ tended first to lower energy and then to higher energy as ρ_P increased from low density to the density of the triple point liquid. However, Messing

* Corresponding author.

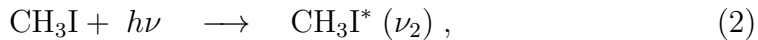
Email address: cherice.evans@qc.cuny.edu (C.M. Evans).

et al. [6,7] did not explore critical temperature effects on $\Delta(\rho_P)$, nor did they correctly account for the vibrational bands on the blue side of the adiabatic Rydberg transition. Messing *et al.* [7] did attempt to model the CH₃I 6s Rydberg transition in argon using a semi-classical statistical line shape function under the assumption that the adiabatic and vibrational transitions have exactly the same line shapes, although no comparison between the experimental spectra and the simulated line shapes was provided. Later researchers [8–10] concentrated on the simulation of the CH₃I 6s Rydberg state doped into argon using both molecular dynamics and semi-classical integral methods. Egorov *et al.* [10] showed that the semi-classical integral method can yield results comparable to the molecular dynamics calculations of Ziegler *et al.* [8,9]. However, none of these authors compared their calculations to experimental measurements obtained along the entire argon number density range.

In this paper we present absorption spectra and a full line shape simulation of the CH₃I 6s and 6s' Rydberg states doped into supercritical argon, krypton and xenon from low perturber number density to the density of the triple point liquid, at both noncritical temperatures and on an isotherm near (i.e., +0.5°C) the critical isotherm of the perturber. Although our simulations use the semi-classical integral method of Messing *et al.* [3,4,6,7], as modified by Egorov *et al.* [10], these calculations represent the first time that the experimental spectra have been successfully modeled across the entire density range using a single set of intermolecular potential parameters. In order to accurately model the complete line shape as a function of perturber number density, we have included both the adiabatic transition



denoted a in Fig. 1, as well as one quantum of the CH_3 deformation vibrational transition ν_2 in the excited state



denoted b , in Fig. 1. A moment analysis is then performed on the simulated adiabatic transition [i.e., eq. (1)] in order to extract the perturber induced shift $\Delta(\rho_P)$ of the adiabatic transition. From these data, we are able to demonstrate that $\Delta(\rho_P)$ increases near the critical density and temperature for both the $6s$ and $6s'$ CH_3I Rydberg states doped into all three atomic perturbers, which is similar to our recent result on the argon critical point effect for the Xe $6s$ and $6s'$ Rydberg transitions [5].

2 Experiment

The dopant methyl iodide (Aldrich, 99.45%) and the perturbers argon (Matheson Tri-gas Inc., 99.9999%), krypton (Matheson Tri-gas Inc., 99.998%), and xenon (Matheson Tri-gas Inc., 99.995%) were used without further purification. The absence of trace impurities in the spectral region of interest was verified by the measurement of individual transmission spectra for each moiety. The pressure and temperature of the sample gas were monitored during the each measurement, allowing the perturber number density to be calculated from the Strobridge equation of state [12] with the parameters given in [13–15]. The CH_3I concentration was optimized for each perturber number density, but was kept under 10ppm for all dopant/perturber samples measured. The gas handling system and the mixing procedures used to ensure a homogeneous sample have been described previously [16]. The gas handling

system was initially baked to a base pressure of 10^{-8} Torr. In order to prevent cross contamination, the gas handling system was allowed to return to the low 10^{-7} Torr range between the addition of the dopant and the perturber gas. The gas handling system was baked back to a base pressure of 10^{-8} Torr before switching to a different dopant/perturber system.

The photoabsorption measurement details have been provided previously [16]. Briefly, monochromatic synchrotron radiation having a resolution of ~ 8 meV in the spectral range of interests was passed through a copper cell equipped with MgF_2 windows (energy cut-off of 10.9 eV at room temperature). This sample cell, which can withstand pressures of up to 100 bar, is equipped with an open flow liquid nitrogen cryostat and resistive heater that allow the temperature to be controlled to $\pm 0.5^\circ\text{C}$ at noncritical temperatures and $\pm 0.2^\circ\text{C}$ near the critical isotherm. To prevent liquid formation in the cell during temperature stabilization, the set point for the critical isotherm was chosen to be 0.5°C above the perturber critical temperature ($T_c = -122.29^\circ\text{C}$ for argon [13]; -63.69°C for krypton [14]; and 16.59°C for xenon [15]). All transmission spectra were normalized both to the incident light intensity and to the empty cell transmission. Once corrected, these spectra were converted to absorbance and normalized to one, in order to allow for comparison with the simulated line shapes.

3 Results and discussion

Selected absorption spectra for the CH_3I $6s$ Rydberg state are presented as a function of perturber number density for noncritical temperatures and on an isotherm near the perturber critical isotherm in Figs. 2 - 4. The analogous

spectra for the $6s'$ Rydberg state are presented in Figs. 5 - 7. These data show that as the perturber number density increases, the ν_2 vibrational band broadens and shifts until it merges with the adiabatic transition. Therefore, determining the perturber induced shift $\Delta(\rho_p)$ of the adiabatic transition from a simple moment analysis of these spectra is not possible. However, if an accurate line shape simulation can be performed, $\Delta(\rho_p)$ for the adiabatic transition can be determined from the moment analysis of the simulated band.

The semi-classical statistical line shape function can be written as a normalized Fourier transform, namely [3,4,10]

$$\mathfrak{L}(\omega) = \frac{1}{2\pi} \text{Re} \int_{-\infty}^{\infty} dt e^{-i\omega t} \langle e^{i\omega(\mathbf{R})t} \rangle, \quad (3)$$

where $\langle \dots \rangle$ represents the thermal average; \mathbf{R} denotes the collection of all dopant/perturber distances; $\omega = \omega(\mathbf{R}) - \omega_0$, with ω_0 being the transition frequency for the neat dopant; and t is the reduced time (i.e., time divided by Planck's constant). Eq. (3) neglects lifetime broadening and assumes that the transition dipole moment is independent of \mathbf{R} . The thermal average can be rewritten as an exponential density expansion [3,4,10]

$$\langle e^{i\omega(\mathbf{R})t} \rangle = \exp [A_1(t) + A_2(t) + \dots], \quad (4)$$

where

$$\begin{aligned} A_n(t) = & \frac{1}{n!} \int \dots \int \prod_{j=1}^n d^3 R_j \mathfrak{F}(\mathbf{R}_1, \dots, \mathbf{R}_n) \\ & \times \prod_{j=1}^n [\exp(-i \Delta V(\mathbf{R}_j) t) - 1] . \end{aligned} \quad (5)$$

In eq. (5), $\mathfrak{F}(\mathbf{R}_1, \dots, \mathbf{R}_n)$ is the Ursell distribution function [3,4,18], and $\Delta V(\mathbf{R}) = V_e(\mathbf{R}) - V_g(\mathbf{R})$, where $V_e(\mathbf{R})$ and $V_g(\mathbf{R})$ are, respectively, the excited and ground state dopant/perturber intermolecular potentials. The Ursell distribu-

tion function for two body interactions [3,4] is $\mathfrak{F}(\mathbf{R}) = \rho_P g_{PD}(\mathbf{R})$, where $g_{PD}(\mathbf{R})$ is the dopant/perturber radial distribution function. The three body Ursell distribution function is estimated using the Kirkwood superposition approximation to be

$$\mathfrak{F}(\mathbf{R}_1, \mathbf{R}_2) = \rho_P^2 [g_{PP}(|\mathbf{R}_1 - \mathbf{R}_2|) - 1] g_{PD}(\mathbf{R}_1) g_{PD}(\mathbf{R}_2) ,$$

where $g_{PP}(\mathbf{R})$ is the perturber/perturber radial distribution function. Substitution of these Ursell distribution functions into eq. (5) gives [3–5]

$$A_1(t) = 4\pi\rho_P \int_0^\infty dr r^2 g_{PD}(r) [e^{-it\Delta V(r)} - 1] , \quad (6)$$

and

$$\begin{aligned} A_2(t) = & 4\pi\rho_P^2 \int_0^\infty dr_1 r_1^2 g_{PD}(r_1) [e^{-it\Delta V(r_1)} - 1] \\ & \times \int_0^\infty dr_2 r_2^2 g_{PD}(r_2) [e^{-it\Delta V(r_2)} - 1] \\ & \times \frac{1}{r_1 r_2} \int_{|r_1-r_2|}^{|r_1+r_2|} s [g_{PP}(s) - 1] ds , \end{aligned} \quad (7)$$

where we have assumed spherical symmetry for the intermolecular potentials. Since the strength of the interaction decreases as the number of bodies involved increases, and since higher order interactions are more difficult to model, our line shape simulations are truncated at $A_2(t)$.

The required radial distribution functions were obtained from the analytical solution of the Ornstein-Zernike equation for a binary system within the Percus-Yevick (PY) closure [19], while the Fourier transform of eq. (3) was performed using a standard fast Fourier transform algorithm [20]. The FFT algorithm requires that eq. (4) be rewritten using Euler's relation as

$$\begin{aligned} Re \left(\langle e^{i\omega(\mathbf{R})t} \rangle \right) &= \exp [Re (A_1(t) + A_2(t))] \cos [Im (A_1(t) + A_2(t))] , \\ Im \left(\langle e^{i\omega(\mathbf{R})t} \rangle \right) &= \exp [Re (A_1(t) + A_2(t))] \sin [Im (A_1(t) + A_2(t))] , \end{aligned} \quad (8)$$

where

$$\begin{aligned}
& \text{Re}[A_1(t) + A_2(t)] \\
&= 4\pi\rho_P \int_0^\infty dr r^2 g_{PD}(r) [\cos(\Delta V(r) t) - 1] \\
&+ 4\pi\rho_P^2 \int_0^\infty \int_0^\infty dr_1 dr_2 h(r_1, r_2) [\cos(\Delta V(r_1) t) \cos(\Delta V(r_2) t) \\
&\quad + 1 - \sin(\Delta V(r_1) t) \sin(\Delta V(r_2) t) \\
&\quad - \cos(\Delta V(r_1) t) - \cos(\Delta V(r_2) t)] , \tag{9}
\end{aligned}$$

and

$$\begin{aligned}
& \text{Im}[A_1(t) + A_2(t)] \\
&= -4\pi\rho_P \int_0^\infty dr r^2 g_{PD}(r) [\sin(\Delta V(r) t)] \\
&- 4\pi\rho_P^2 \int_0^\infty \int_0^\infty dr_1 dr_2 h(r_1, r_2) [\sin(\Delta V(r_1) t) \cos(\Delta V(r_2) t) \\
&\quad + \cos(\Delta V(r_1) t) \sin(\Delta V(r_2) t) \\
&\quad - \sin(\Delta V(r_1) t) - \sin(\Delta V(r_2) t)] , \tag{10}
\end{aligned}$$

with

$$h(r_1, r_2) = r_1 g_{PD}(r_1) r_2 g_{PD}(r_2) \int_{|r_1-r_2|}^{|r_1+r_2|} s [g_{PP}(s) - 1] ds .$$

The line shape obtained from the transform of eq. (3), using eqs. (8) - (10), was convoluted with a standard Gaussian slit function to account for the finite (~ 8 meV) resolution of the monochromator.

Eqs. (3) - (10) are explicitly dependent on the excited and ground state perturber/dopant intermolecular potentials through $\Delta V(r)$, and are implicitly dependent on the perturber/perturber and perturber/dopant ground state intermolecular potential via $g_{PP}(r)$ and $g_{PD}(r)$. Thus, these simulations require one to develop a single set of ground state and excited state intermolecular potential parameters for each system. A standard Lennard-Jones 6-12 poten-

tial

$$V(r) = 4\varepsilon \left[\left(\frac{\sigma}{r} \right)^{12} - \left(\frac{\sigma}{r} \right)^6 \right], \quad (11)$$

was chosen for all of the perturber/perturber ground state intermolecular interactions (i.e., Ar/Ar, Kr/Kr, Xe/Xe), while all of the ground state dopant/perturber intermolecular interactions (i.e., CH₃I/Ar, CH₃I/Kr, and CH₃I/Xe) were modeled using a modified Stockmeyer potential,

$$V(r) = 4\varepsilon' \left[\left(\frac{\sigma'}{r} \right)^{12} - \left(\frac{\sigma'}{r} \right)^6 \right] - \frac{1}{r^6} \alpha_P \mu_D^2, \quad (12)$$

which can be rewritten in standard Lennard-Jones 6-12 potential form [17], with $\varepsilon = \varepsilon' \left[1 + \alpha_P \mu_D^2 / 4\varepsilon' \sigma'^6 \right]^2$ and $\sigma = \sigma' \left[1 + \alpha_P \mu_D^2 / 4\varepsilon' \sigma'^6 \right]^{-1/6}$. (One should note that the modified Stockmeyer potential includes orientational effects via an angle average that presumes the free rotation of CH₃I [21].)

Finally, an exponential-6 potential, given by

$$V(r) = \frac{\varepsilon}{1 - (6/\gamma)} \left\{ \frac{6}{\gamma} e^{\gamma(1-\chi)} - \chi^{-6} \right\}, \quad (13)$$

was chosen for all excited state dopant/ground state perturber interactions. In eqs. (11) - (13), ε (or ε') is the well-depth, σ (or σ') is the collision parameter, α_P is the perturber polarizability, μ_D is the dopant dipole moment, $\chi \equiv r/r_e$ (where r_e is the equilibrium distance), and γ is the potential steepness. The parameters for all three dopant/perturber data sets were adjusted by hand in a consistent manner to give the best simulated line shape in comparison to our experimental spectra throughout the entire perturber density range, although the perturber/perturber and dopant/perturber ground state potential parameters used are in accord with those employed in our earlier studies of the quasi-free electron energy in rare gas perturbers [17]. All parameter values for both the adiabatic transition and the ν_2 CH₃I excited state vibrational transition are given in Table 1. The relative intensities of the simulated bands were

fixed by comparison to the absorption spectra of CH₃I at perturber number densities where all bands (i.e. the adiabatic and vibrational transitions) could be clearly identified. Experimentally, at low perturber number densities the ratio of the vibrational band intensity to the adiabatic transition intensity is 0.22 for both the CH₃I 6s and 6s' Rydberg states in all three perturbers.

The dotted lines in Figs. 2 - 4 show the best fit to experiment for the CH₃I 6s absorption, and in Figs. 5 - 7 for the 6s' absorption. Clearly, the simulated spectra closely match the experimental spectra for all densities. Both the simulated and experimental line shapes exhibit a slight shift to lower energies at low perturber number densities, followed by a strong shift to higher energies at high perturber number densities, similar to the original observations of Messing *et al.* [6,7]. [Experimental spectra of CH₃I in Xe at number densities between $5.0 \times 10^{21} \text{ cm}^{-3}$ and $7.0 \times 10^{21} \text{ cm}^{-3}$ could not be obtained, because of the large density deviation induced by small temperature fluctuations ($\sim 2.0 \times 10^{21} \text{ cm}^{-3}$ for a 0.001°C temperature change) in this density region.]

Given these accurate simulations, a moment analysis was performed to determine the perturber induced shift $\Delta(\rho_P)$ of the adiabatic transition. $\Delta(\rho_P)$ was approximated as the first moment [3,4]

$$\Delta(\rho_P) \equiv M_1 = \int \mathfrak{L}(E) E dE \Big/ \int \mathfrak{L}(E) dE \quad , \quad (14)$$

where $\mathfrak{L}(E)$ is the simulated absorption band for the adiabatic transition and $E = \hbar(\omega - \omega_0)$ ($\hbar \equiv$ reduced Planck constant). The first moment of the simulated CH₃I 6s adiabatic transition is plotted as a function of the reduced perturber number density ρ_r (where $\rho_r = \rho/\rho_c$, with $\rho_c \equiv$ critical density of the perturber) in Fig. 8, and in Fig. 9 for the 6s' transition. The first

moment of the simulated adiabatic band does not red shift at low perturber density, as was originally stated by Messing *et al.* [6,7]. This absence of a red shift is caused by the blue degradation of the adiabatic transition, which places the average energy (i.e., the first moment) of the band to the high energy side of the absorption maximum. The ground state interaction between CH₃I and the perturber is attractive, and therefore the ground state of the dopant is stabilized by the perturber solvent shell. The slight red shift of the absorption maximum observed at low perturber number densities indicates that the CH₃I excited states are also stabilized by the perturber solvent shell. As the density increases, however, perturber molecules begin to shield the optical electron from the CH₃I cationic core, thereby increasing the excitation energy of the optical electron. Thus, as the perturber density increases, the energy of the excited state also increases, leading to a blue shift at higher perturber densities.

The $6s$ and $6s'$ Rydberg states correspond to an optical electron in the same Rydberg orbital, but with the cation in a different core state: $J = 3/2$ for s and $J = 1/2$ for s' , where J is the total angular momentum of the core. In our recent investigation of $\Delta(\rho_p)$ for Xe in Ar [5], we found that $\Delta(\rho_p)$ of the $6s$ transition is 0.2 eV larger than that for the $6s'$ transition, indicating that the change in the core quadrupole moment affects the dopant/perturber interactions in a dense perturbing medium. However, $\Delta(\rho_p)$ for the CH₃I $6s$ and $6s'$ Rydberg transitions near the triple point density are identical to within experimental error for the perturbors argon and krypton, and differ only slightly (i.e., 30 meV) for CH₃I in xenon. The insensitivity of these CH₃I/perturber systems to the change in the CH₃I cationic core is probably caused by the large permanent dipole moment of CH₃I, which masks the effect of the quadrupole

moment. Xenon, however, is extremely sensitive to electric fields because of its large polarizability. Therefore, the slight difference between the xenon induced shifts of the CH₃I 6s and 6s' Rydberg transitions may well be caused by small changes in the permanent dipole moment of CH₃I influencing changes in the induced dipole or local quadrupoles in the xenon perturber.

A critical point effect on the 6s and 6s' transition energies is also apparent in Figs. 8 and 9 for all three perturbers. The CH₃I 6s adiabatic transition in argon is blue-shifted by 20 meV near the critical temperature and critical density, while those in krypton and xenon are blue-shifted by 30 meV and 15 meV, respectively. Identical results are obtained for the CH₃I 6s' adiabatic transitions in argon and krypton. However, a smaller critical point effect of 5 meV is observed for the CH₃I 6s' transition in xenon, which is related to the smaller overall blue shift of the CH₃I 6s' transition in comparison to the 6s transition. It is interesting to note that the critical isotherm turning points that bound the perturber phase diagram saddle point (pressure versus number density) coincide with those number densities that delimit the deviation of the first moment from the noncritical isotherm curve. As the perturber approaches its critical point, the clustering around dopant atoms or molecules increases due to an increase in the correlation length of the perturber. This change in solvation around a solute in a supercritical fluid has been observed in a variety of other spectroscopic systems [2,22], as well as in partial molar volume experiments [22].

In the low to medium density range, the energy of the absorption maximum for the 6s and 6s' CH₃I Rydberg states has a larger red shift in xenon, which is caused by the larger xenon polarizability. The CH₃I Rydberg states also broaden more quickly in xenon. This increased broadening is probably due to

a combination of increased xenon polarizability and an increase in the probability of collisional de-excitation due to the size of xenon. However, $\Delta(\rho_P)$ is larger for argon than for krypton and xenon. This change is caused by an overall decrease in the total number of perturber atoms within the first solvent shell surrounding the CH₃I dopant as the perturber atoms become larger. The variation in the critical point effect, with krypton having a larger effect than argon and xenon, is caused by the strength of the perturber/CH₃I interactions in comparison to the perturber/perturber interactions, coupled with the differences in the ground and excited state dopant/perturber interaction potentials. The CH₃I/Kr ground state potential well-depth is close (i.e., 24 K) to the Kr/Kr potential well-depth. This implies that the CH₃I/Kr interactions near the krypton critical point will be comparable to the Kr/Kr interactions, thereby leading to a large increase in the local perturber density near the critical point of the perturber, and a larger critical effect. Similarly the critical point effect decreases as one goes from krypton to argon to xenon because the difference in well-depth for all intermolecular potentials increases.

In summary, we have shown that the absorption line shapes of low- n molecular Rydberg transitions doped into atomic perturbers can be accurately simulated across a broad perturber density range with an appropriate choice of intermolecular potentials and a single set of potential parameters for each perturber. Moment analyses of the simulated CH₃I adiabatic transitions exhibited a clear critical point effect in all CH₃I/perturber systems investigated. Finally, a general discussion of the density dependence of the line shapes and moment analyses was provided by comparing the various dopant/perturber systems.

Acknowledgements

All experimental measurements were made at the University of Wisconsin Synchrotron Radiation Center (NSF DMR-0084402), with support from the Petroleum Research Fund (PRF#45728-B6), the Professional Staff Congress - City University of New York and the Louisiana Board of Regents Support Fund (LEQSF(2006-09)-RD-A-33).

References

- [1] M. B. Robin, Higher Excited States of Polyatomic Molecules Vol.I-Vol.III, Academic Press, New York, 1974, 1975, 1985, and references therein.
- [2] S. C. Tucker, Chem. Rev. 99 (1999) 391, and references therein.
- [3] I. Messing, B. Raz, J. Jortner, J. Chem. Phys. 66 (1977) 2239 .
- [4] I. Messing, B. Raz, J. Jortner, J. Chem. Phys. 66 (1977) 4577.
- [5] Luxi Li, Xianbo Shi, C. M. Evans, G. L. Findley, Chem. Phys. Lett. 461 (2008) 207.
- [6] I. Messing, B. Raz, J. Jortner, Chem. Phys. 25 (1977) 55.
- [7] I. Messing, B. Raz, J. Jortner, Chem. Phys. 23 (1977) 351.
- [8] T. Kalbfleisch, R. Fan, J. Roebber, P. Moore, E. Jacobsen, L.D. Ziegler, J. Chem. Phys. 103 (1995) 7673.
- [9] R. Fan, T. Kalbfleisch, L.D. Ziegler, J. Chem. Phys. 104 (1996) 3886.
- [10] S.A. Egorov, M.D. Stephens, J.L. Skinner, J. Chem. Phys. 107 (1997) 10485.
- [11] P. Larrégaray, A. Cavina, M. Chergui, Chem. Phys. 308 (2005) 13.

- [12] T.R. Strobridge, NBS Tech. Note 129C, Washington, DC, 1962.
- [13] A.L. Gosman, R.D. McCarty, J.G. Hust, NSRD-NBS (1969) 27.
- [14] W.B. Streett, L.A.K. Staveley, J. Chem. Phys. 55 (1971) 2495.
- [15] W.B. Streett, L.S. Sagan, L.A.K. Staveley, J. Chem. Thermodynamics 5 (1973) 633.
- [16] C.M. Evans, Ph.D Dissertation, Louisiana State University, Baton Rouge, LA, 2001; see also C. M. Evans, J. D. Scott, and G. L. Findley, Rec. Res. Chem. Phys. 3 (2002) 351.
- [17] C.M.Evans, G.L.Findley, Phys. Rev. A 72 (2005) 022717; see also Xianbo Shi, Luxi Li, C.M. Evans, and G.L. Findley, Nucl. Inst. Meth. A 582 (2007) 270, and references therein.
- [18] J.K. Percus, in: H.L. Frisch, S.L. Lebowitz (Eds.) Classical Fluids, Benjamin, New York, 1964.
- [19] E.W. Grundke, D. Henderson, R.D. Murphy, Can. J. Phys. 51 (1973) 1216.
- [20] W.H. Press, S.A. Teukolsky, W.T. Vetterling, B.P. Flannery, Numerical Recipes in FORTRAN: The Art of Scientific Computing, Cambridge University Press, New York, 1992.
- [21] J. O. Hirschfelder, C. F. Curtiss, R. B. Bird, Molecular Theory of Gases and Liquids, Wiley, New York, 1954.
- [22] O. Kajimoto, Chem. Rev. 99 (1999) 355, and references therein.

Table captions

Table 1. Intermolecular potential parameters for all dopant/perturber systems.

Figure captions

Fig. 1. Experimental absorbance (relative units) of CH₃I 6s and 6s' doped into Ar at an argon number density of $\rho_{\text{Ar}} = 1.89 \times 10^{21} \text{ cm}^{-3}$ and a temperature of -79.8°C. *a* corresponds to eq. (1), *b* to eq. (2). For the 6s Rydberg state, $E_0 = 6.154 \text{ eV}$; for the 6s' Rydberg state, $E_0 = 6.767 \text{ eV}$.

Fig. 2. Selected experimental absorbance (—, relative units) and simulated line shapes (⋯) for the CH₃I 6s Rydberg transition in argon at (a) noncritical temperatures and (b) on an isotherm (-121.8°C) near the critical isotherm. The data are offset vertically by the argon perturber number density ρ_{Ar} . The transition energy is $E_0 = 6.154 \text{ eV}$ for the unperturbed CH₃I 6s Rydberg transition. The variation between experiment and simulation on the high energy side is caused by other vibrational transitions and by perturber dependent lifetime broadening not modeled here. (While all spectra have been normalized to 1 for comparison with the simulated line shapes, the integrated intensity is independent of the perturber number density.)

Fig. 3. Select experimental absorbance (—, relative units) and simulated line shapes (⋯) for the CH₃I 6s Rydberg transition in krypton at (a) noncritical temperatures and (b) on an isotherm (-63.3°C) near the critical isotherm. The data are offset vertically by the krypton perturber number density ρ_{Kr} . The transition energy is $E_0 = 6.154 \text{ eV}$ for the unperturbed CH₃I 6s Rydberg transition. The variation between experiment and simulation on the high

energy side is caused by other vibrational transitions and by perturber dependent lifetime broadening not modeled here. (While all spectra have been normalized to 1 for comparison with the simulated line shapes, the integrated intensity is independent of the perturber number density.)

Fig. 4. Selected experimental absorbance (—, relative units) and simulated line shapes (\cdots) for the CH₃I 6s Rydberg transition in xenon at (a) noncritical temperatures and (b) on an isotherm (17.0°C) near the critical isotherm. The data are offset vertically by the xenon perturber number density ρ_{Xe} . The transition energy is $E_0 = 6.154$ eV for the unperturbed CH₃I 6s Rydberg transition. The variation between experiment and simulation on the high energy side is caused by other vibrational transitions and by perturber dependent lifetime broadening not modeled here. (While all spectra have been normalized to 1 for comparison with the simulated line shapes, the integrated intensity is independent of the perturber number density.)

Fig. 5. Selected experimental absorbance (—, relative units) and simulated line shapes (\cdots) for the CH₃I 6s' Rydberg transition in argon at (a) noncritical temperatures and (b) on an isotherm (-121.8°C) near the critical isotherm. The data are offset vertically by the argon perturber number density ρ_{Ar} . The transition energy is $E_0 = 6.767$ eV for the unperturbed CH₃I 6s' Rydberg transition. The variation between experiment and simulation on the high energy side is caused by other vibrational transitions and by perturber dependent lifetime broadening not modeled here. (While all spectra have been normalized to 1 for comparison with the simulated line shapes, the integrated intensity is independent of the perturber number density.)

Fig. 6. Selected experimental absorbance (—, relative units) and simulated line shapes (\cdots) for the CH_3I $6s'$ Rydberg transition in krypton at (a) noncritical temperatures and (b) on an isotherm (-63.3°C) near the critical isotherm. The data are offset vertically by the krypton perturber number density ρ_{Kr} . The transition energy is $E_0 = 6.767$ eV for the unperturbed CH_3I $6s'$ Rydberg transition. The variation between experiment and simulation on the high energy side is caused by other vibrational transitions and by perturber dependent lifetime broadening not modeled here. (While all spectra have been normalized to 1 for comparison with the simulated line shapes, the integrated intensity is independent of the perturber number density.)

Fig. 7. Selected experimental absorbance (—, relative units) and simulated line shapes (\cdots) for the CH_3I $6s'$ Rydberg transition in xenon at (a) noncritical temperatures and (b) on an isotherm (17.0°C) near the critical isotherm. The data are offset vertically by the xenon perturber number density ρ_{Xe} . The transition energy is $E_0 = 6.767$ eV for the unperturbed CH_3I $6s'$ Rydberg transition. The variation between experiment and simulation on the high energy side is caused by other vibrational transitions and by perturber dependent lifetime broadening not modeled here. (While all spectra have been normalized to 1 for comparison with the simulated line shapes, the integrated intensity is independent of the perturber number density.)

Fig. 8. (a) The perturber induced shift Δ , as approximated by a moment analysis [i.e., eq. (14)], of the simulated primary transition for the CH_3I $6s$ Rydberg state as a function of the reduced perturber number density ρ_r ($\rho_r \equiv \rho/\rho_c$, $\rho_c \equiv$ perturber critical density) for argon, krypton and xenon. (\bullet), simulations obtained at noncritical temperatures; (\circ), simulations near the critical isotherm. (b) An expanded view of Δ near the perturber critical point. $\rho_c = 8.0 \times 10^{21}$

cm^{-3} for argon [13], $\rho_c = 6.6 \times 10^{21} \text{ cm}^{-3}$ for krypton [14] and $\rho_c = 5.0 \times 10^{21} \text{ cm}^{-3}$ for xenon [15]. The solid lines provide a visual aid. See text for discussion.

Fig. 9. The perturber induced shift Δ , as approximated by a moment analysis [i.e., eq. (14)], of the simulated primary transition for the $\text{CH}_3\text{I } 6s'$ Rydberg state as a function of the reduced perturber number density ρ_r . See the caption of Fig. 8.

Table 1
 Intermolecular potential parameters for all dopant/perturber systems.

	ε/k_B (K)	r_e (Å)	γ
Ar/Ar	119.5	3.826 ^a	–
Kr/Kr	172.7	4.031 ^a	–
Xe/Xe	229.0	4.552 ^a	–
CH ₃ I/Ar	162.2	4.572 ^a	–
CH ₃ I/Kr	196.7	4.676 ^a	–
CH ₃ I/Xe	297.46	4.896 ^a	–
CH ₃ I 6s/Ar	110.0	6.300	12.75
CH ₃ I 6s/Kr	245.0	6.200	11.30
CH ₃ I 6s/Xe	400.0	6.390	10.25
CH ₃ I 6s ν_2 /Ar	150.0	6.300	12.15
CH ₃ I 6s ν_2 /Kr	225.0	6.300	10.75
CH ₃ I 6s ν_2 /Xe	360.0	6.500	9.50
CH ₃ I 6s'/Ar	110.0	6.300	12.75
CH ₃ I 6s'/Kr	245.0	6.200	11.30
CH ₃ I 6s'/Xe	400.0	6.290	10.25
CH ₃ I 6s' ν_2 /Ar	150.0	6.300	12.15
CH ₃ I 6s' ν_2 /Kr	225.0	6.300	10.75
CH ₃ I 6s' ν_2 /Xe	360.0	6.350	9.50

^aFor a Lennard-Jones 6-12 potential, $\sigma = 2^{-1/6}r_e$.

Fig. 1. Experimental absorbance (relative units) of CH₃I 6s and 6s' doped into Ar at an argon number density of $\rho_{\text{Ar}} = 1.89 \times 10^{21} \text{ cm}^{-3}$ and a temperature of -79.8°C . *a* corresponds to eq. (1), *b* to eq. (2). For the 6s Rydberg state, $E_0 = 6.154 \text{ eV}$; for the 6s' Rydberg state, $E_0 = 6.767 \text{ eV}$.

Fig. 2. Selected experimental absorbance (—, relative units) and simulated line shapes (⋯) for the CH₃I 6s Rydberg transition in argon at (a) noncritical temperatures and (b) on an isotherm (-121.8°C) near the critical isotherm. The data are offset vertically by the argon perturber number density ρ_{Ar} . The transition energy is $E_0 = 6.154 \text{ eV}$ for the unperturbed CH₃I 6s Rydberg transition. The variation between experiment and simulation on the high energy side is caused by other vibrational transitions and by perturber dependent lifetime broadening not modeled here. (While all spectra have been normalized to 1 for comparison with the simulated line shapes, the integrated intensity is independent of the perturber number density.)

Fig. 3. Select experimental absorbance (—, relative units) and simulated line shapes (⋯) for the CH₃I 6s Rydberg transition in krypton at (a) noncritical temperatures and (b) on an isotherm (-63.3°C) near the critical isotherm. The data are offset vertically by the krypton perturber number density ρ_{Kr} . The transition energy is $E_0 = 6.154 \text{ eV}$ for the unperturbed CH₃I 6s Rydberg transition. The variation between experiment and simulation on the high energy side is caused by other vibrational transitions and by perturber dependent lifetime broadening not modeled here. (While all spectra have been normalized to 1 for comparison with the simulated line shapes, the integrated intensity is independent of the perturber number density.)

Fig. 4. Selected experimental absorbance (—, relative units) and simulated line shapes (⋯) for the CH₃I 6s Rydberg transition in xenon at (a) noncritical temperatures and (b) on an isotherm (17.0°C) near the critical isotherm. The data are offset vertically by the xenon perturber number density ρ_{Xe} . The transition energy is $E_0 = 6.154 \text{ eV}$ for the unperturbed CH₃I 6s Rydberg transition. The variation between experiment and simulation on the high energy side is caused by other vibrational transitions and by perturber dependent lifetime broadening not modeled here. (While all spectra have been normalized to 1 for comparison with the simulated line shapes, the integrated intensity is independent of the perturber number density.)

Fig. 5. Selected experimental absorbance (—, relative units) and simulated line shapes (\cdots) for the $\text{CH}_3\text{I } 6s'$ Rydberg transition in argon at (a) noncritical temperatures and (b) on an isotherm (-121.8°C) near the critical isotherm. The data are offset vertically by the argon perturber number density ρ_{Ar} . The transition energy is $E_0 = 6.767$ eV for the unperturbed $\text{CH}_3\text{I } 6s'$ Rydberg transition. The variation between experiment and simulation on the high energy side is caused by other vibrational transitions as well as perturber dependent lifetime broadening that are not modeled here. (All experimental data have been normalized to 1 in order to allow for comparison with the simulated line shapes.)

Fig. 6. Selected experimental absorbance (—, relative units) and simulated line shapes (\cdots) for the $\text{CH}_3\text{I } 6s'$ Rydberg transition in krypton at (a) noncritical temperatures and (b) on an isotherm (-63.3°C) near the critical isotherm. The data are offset vertically by the krypton perturber number density ρ_{Kr} . The transition energy is $E_0 = 6.767$ eV for the unperturbed $\text{CH}_3\text{I } 6s'$ Rydberg transition. The variation between experiment and simulation on the high energy side is caused by other vibrational transitions and by perturber dependent lifetime broadening not modeled here. (While all spectra have been normalized to 1 for comparison with the simulated line shapes, the integrated intensity is independent of the perturber number density.)

Fig. 7. Selected experimental absorbance (—, relative units) and simulated line shapes (\cdots) for the $\text{CH}_3\text{I } 6s'$ Rydberg transition in xenon at (a) noncritical temperatures and (b) on an isotherm (17.0°C) near the critical isotherm. The data are offset vertically by the xenon perturber number density ρ_{Xe} . The transition energy is $E_0 = 6.767$ eV for the unperturbed $\text{CH}_3\text{I } 6s'$ Rydberg transition. The variation between experiment and simulation on the high energy side is caused by other vibrational transitions and by perturber dependent lifetime broadening not modeled here. (While all spectra have been normalized to 1 for comparison with the simulated line shapes, the integrated intensity is independent of the perturber number density.)

Fig. 8. (a) The perturber induced shift Δ , as approximated by a moment analysis [i.e., eq. (14)], of the simulated primary transition for the $\text{CH}_3\text{I } 6s$ Rydberg state as a function of the reduced perturber number density ρ_r ($\rho_r \equiv \rho/\rho_c$, $\rho_c \equiv$ perturber critical density) for argon, krypton and xenon. (\bullet), simulations obtained at non-critical temperatures; (\circ), simulations near the critical isotherm. (b) An expanded view of Δ near the perturber critical point. $\rho_c = 8.0 \times 10^{21} \text{ cm}^{-3}$ for argon [13], $\rho_c = 6.6 \times 10^{21} \text{ cm}^{-3}$ for krypton [14] and $\rho_c = 5.0 \times 10^{21} \text{ cm}^{-3}$ for xenon [15]. The solid lines provide a visual aid. See text for discussion.

Fig. 9. The perturber induced shift Δ , as approximated by a moment analysis [i.e., eq. (14)], of the simulated primary transition for the CH₃I 6*s*' Rydberg state as a function of the reduced perturber number density ρ_r . See the caption of Fig. 8.